

EES Solar

Accepted Manuscript

This article can be cited before page numbers have been issued, to do this please use: L. M. van der Poll, M. Camara Diaz, R. K. Boekhoff, P. Vageeswaran, N. van Silfhout, L. Mazzarella, S. Ganapathy, L. Bannenberg, D. Ghosh, A. H. M. Smets and T. J. Savenije, *EES Sol.*, 2026, DOI: 10.1039/D6EL00044D.



This is an Accepted Manuscript, which has been through the Royal Society of Chemistry peer review process and has been accepted for publication.

Accepted Manuscripts are published online shortly after acceptance, before technical editing, formatting and proof reading. Using this free service, authors can make their results available to the community, in citable form, before we publish the edited article. We will replace this Accepted Manuscript with the edited and formatted Advance Article as soon as it is available.

You can find more information about Accepted Manuscripts in the [Information for Authors](#).

Please note that technical editing may introduce minor changes to the text and/or graphics, which may alter content. The journal's standard [Terms & Conditions](#) and the [Ethical guidelines](#) still apply. In no event shall the Royal Society of Chemistry be held responsible for any errors or omissions in this Accepted Manuscript or any consequences arising from the use of any information it contains.

Broader context statement

As the world transitions toward sustainable energy, solar power is playing an increasingly important role, driven by its abundance, scalability, and position among the most cost-effective sources of electricity. However, meeting rising energy demand requires solar cells with efficiencies beyond the limits of conventional technologies. Metal halide perovskites have emerged as contenders, rivaling silicon in performance. Their electronic properties are tunable, enabling the design of multi-absorber solar cells

In this context, low bandgap perovskites are needed to harvest low-energy light, while reducing toxic lead content and developing scalable, industry-ready fabrication methods remain critical challenges. Here, we partially replace lead with tin to lower toxicity and achieve the desired bandgap. We deposit the films by thermal evaporation in vacuum. The precursors spontaneously mix after deposition, forming the desired perovskite phase. This enables the use of two precursor layers, whereas other lead-based perovskite compositions require multiple deposition cycles. However, post-deposition thermal annealing remains crucial to obtain highly crystalline, compositionally homogeneous films with low defect densities and excellent charge transport properties. Our findings advance understanding of the conversion in thermally evaporated low bandgap tin lead perovskites and demonstrate a viable and scalable route towards commercial perovskite solar cells.



ARTICLE

Interplay of Diffusion and Crystallization in Sequentially Evaporated Lead Tin Perovskites

Lara M. van der Poll,^a Moisés Cámara Díaz,^a Reinder K. Boekhoff,^b Poojalakshmi Vageeswaran,^c Niels van Silfhout,^a Luana Mazzarella,^b Swapna Ganapathy,^d Lars J. Bannenberg,^d Dibyajyoti Ghosh,^c Arno H.M. Smets,^b and Tom J. Savenije^{*a}Received 00th January 20xx,
Accepted 00th January 20xx

DOI: 10.1039/x0xx00000x

Low bandgap (LBG) Pb-Sn perovskites (PVKs) are key absorber materials for high-efficiency all-perovskite tandem solar cells. Yet, their fabrication at device-relevant thicknesses with high structural and optoelectronic quality remains challenging. Here, we demonstrate the scalable deposition of formamidinium lead tin triiodide (FAPb_{0.5}Sn_{0.5}I₃) films up to 700 nm thick using a single cycle of sequential thermal evaporation (1c-sTE). The process relies on vacuum deposition of a PbSn₄ alloy followed by FAI, without the need for additives typically used in solution processing. Optical spectroscopy, XRD, solid-state NMR, and TRMC measurements reveal that FAI readily diffuses into the inorganic precursor layer even at room temperature. Independent of the precursor mixing time, annealing is required to achieve films with increased local homogeneity, large grains, and high crystallinity, leading to reduced defect density, increased carrier mobility up to 80 cm²/(Vs), and lifetimes close to a microsecond. The resulting films are stoichiometrically uniform across their thickness and exhibit dense, columnar grain morphologies. A device with the architecture ITO/PEDOT:PSS/FAPb_{0.5}Sn_{0.5}I₃/C60/BCP/Ag, shows power conversion efficiencies of 10%, with voltage losses mainly at the PEDOT:PSS/PVK interface. This work demonstrates that 1c-sTE is a feasible method for producing LBG Pb-Sn PVK films suitable for PV applications.

Introduction

Metal halide perovskites (PVKs) have emerged as highly promising absorber layers in single-junction solar cells, resulting in efficiency records exceeding 27%.^[1] Their integration into perovskite solar cells (PSCs) is facilitated by their desirable optoelectronic properties for photovoltaic (PV) applications, including tunable bandgaps, relatively high absorption coefficients, and defect tolerance.

A considerable amount of research on PSCs is devoted to combining PVKs with silicon or with PVKs of differing bandgaps to enhance the utilization of the solar spectrum and thereby maximize the power conversion efficiency (PCE).^[2-5] All-PVK tandems require a combination of wide bandgap (WBG, ~1.7-1.8 eV) and low bandgap (LBG, ~1.2-1.3 eV) PVK absorber layers, which are engineered by modifying the composition of the characteristic ABX₃ structure. WBG perovskites are formed by partially substituting iodide (I⁻) with bromide (Br⁻) at the X-site, while LBG PVKs are achieved by replacing lead (Pb²⁺) with tin

(Sn²⁺) at the B-site. The A-site, occupied by monovalent cations, such as methylammonium (MA⁺), formamidinium (FA⁺), and cesium (Cs⁺), mainly stabilizes the crystal structure with minimal impact on the bandgap.

Today, PVK thin films are still mostly produced from solution. In this process, the precursors are dissolved in a common, often toxic, solvent and, at the lab scale, typically deposited by spincoating. Industrial PVK production from solution has been demonstrated using scalable techniques, such as slot-die coating, blade coating, and inkjet printing.^[6-9] Yet, achieving high crystallinity and uniformity in large-area films remains challenging due to the complex dynamics during film formation. For LBG PVKs, various additives are used to mediate crystallization, suppress oxidation, and achieve the desired film phase and morphology. However, these additives can introduce new defects, leading to performance losses, and may also compromise device stability if not carefully optimized.^[10-13]

Alternatively, PVK layers can be produced by physical vapor deposition in vacuum, e.g., thermal evaporation (TE). This technique has garnered increased attention in recent years due to its scalability, adaptability, and ability to uniformly coat textured surfaces.^[13-15] These traits make it a highly suitable method specifically to produce multi-layered device architectures. Two primary modes of TE are used: coevaporation (cTE) and sequential evaporation (sTE). In cTE, all precursors are deposited simultaneously, and compositional control is achieved by tuning the ratio of the individual precursor sublimation rates. cTE is enticing for industry due to

^a Department of Chemical Engineering, Delft University of Technology, the Netherlands. Email: t.j.savenije@tudelft.nl

^b Department of Electrical Sustainable Energy, Delft University of Technology, the Netherlands

^c Department of Materials Science and Engineering and Department of Chemistry, Indian Institute of Technology, New Delhi, India

^d Reactor Institute Delft, Delft University of Technology, Delft, Netherlands

Supplementary Information available: [details of any supplementary information available should be included here]. See DOI: 10.1039/x0xx00000x



the fast deposition speeds that are possible. However, achieving stoichiometric films is complex due to rate- and pressure-dependent interactions between the precursor streams.^[16,17] Despite these challenges, cTE has repeatedly enabled the fabrication of 1-j PSCs with efficiencies beyond 20%.^[18-20] Contrary to cTE, sTE involves the stepwise deposition of the separate precursors in a layer-by-layer approach. This method is comparatively simpler than cTE, offering improved control over the film stoichiometry and greater reproducibility, albeit with longer processing times. Like cTE, sTE has aided in the production of 1-j lead-based PSCs with a PCE of 24%.^[21]

It has been shown that producing LBG PVKs in vacuum conditions yields high-quality thin films.^[22-25] Notably, TE offers a significant advantage by inherently suppressing the oxidation of tin(II) to tin(IV) during processing. This reaction opens degradation pathways that severely inhibit cell performance and readily occur in the presence of oxygen, moisture, and other impurities. These factors are difficult to eliminate in a solvent-based process, and additives such as tin(II) fluoride (SnF₂) are frequently incorporated to mitigate the aftermath of tin(II) oxidation.^[26-28] Focusing specifically on the TE of LBG perovskites, cTE has been successfully employed to fabricate single-junction PSCs with power conversion efficiencies of up to 14%. These efficiencies are relatively low compared to the state-of-the-art spincoated devices, which have achieved champion efficiencies of around 24%.^[29] However, those devices have undergone extensive optimization over many years of research. To date, no LBG devices fabricated via sTE have been reported.

To achieve adequate light absorption, and thus optimal charge-generation density, the PVK layer must be 500-700 nm thick.^[25] However, earlier work on Pb-based PVKs has reported that using sTE imposes an upper limit on the film thickness achievable in a single deposition cycle, a restriction attributed to limited interdiffusion of the deposited precursor layers. To overcome this, multi-cycle sTE was developed, where each cycle (c) consists of a full sequence of depositing all separate precursors.^[30]

In this work, we report the successful deposition of LBG formamidinium lead tin triiodide (FAPb_{0.5}Sn_{0.5}I₃) films up to 700 nm using a single cycle (1c) of sTE. This method first involves the deposition of an in-house-prepared PbI₂-SnI₂ alloy layer, referred to as PbSnI₄, followed by a layer of formamidinium iodide (FAI). This approach produces near-intrinsic perovskites while eliminating the need for the additives that are normally required for solution-processed PVKs.^[22] The resulting films are compositionally uniform throughout their thickness and display compact structures and well-defined columnar grains. By integrating these layers into functioning PSCs, achieving champion PCEs above 10%, we underscore the viability of 1c-sTE for scalable PVK absorber production.

Central to this study is understanding why this material can be produced in 1 cycle of sTE at such thicknesses. To address this, the differences between samples produced in a single cycle and

those from a double cycle (2c) were examined, revealing that the 1c films exhibit superior structural and optoelectronic properties compared to their 2c counterparts. Furthermore, we thoroughly investigate the interdiffusion behavior of the PbSnI₄ and FAI precursor layers by characterizing the films at three stages during the production, both before and after annealing, using XRD, XPS, and solid-state NMR. Density-functional theory (DFT) calculations further reveal that the alloy is only weakly stabilized relative to its precursors and is energetically close to the mixed perovskite phase, facilitating lattice disruption and efficient interdiffusion. Finally, by comparing XRD and TRMC data of samples subjected to different annealing procedures, we establish that the diffusion of the precursors is not hindered by the concurrent crystallization into PVKs.

Experimental

PbSnI₄ alloy preparation

In an N₂-filled glovebox, tin(II) iodide beads (SnI₂, 99.999%) were ground and mixed with lead(II) iodide (PbI₂, 99.99%) in a 1:1 mol ratio. The mixture was transferred from the glovebox into the evaporator through ambient air. Afterward, the evaporation chamber was pumped down to 10⁻⁶ mbar and maintained in a vacuum overnight. Subsequently, an Ar flow was established through the chamber, and the crucible containing the mixture was slowly heated to 420 °C. After 20 minutes, the crucible was cooled to room temperature. The resulting alloy, denoted as PbSnI₄, was used in the perovskite deposition without further treatment.

Sequential thermal evaporation of perovskite layers

Quartz substrates were subsequently washed with acetone and isopropanol in an ultrasonic bath. Next, they were treated with oxygen plasma for 10 minutes. After loading them into the evaporation chamber, the substrates were swiftly heated to 40 °C in vacuum (10⁻⁷ - 10⁻⁶ mbar) to ensure the removal of residual adherents. For the deposition of FAPb_{0.5}Sn_{0.5}I₃, sequential layers of PbSnI₄ and formamidinium iodide (FAI, 99.99%) were deposited onto a rotating substrate. The thicknesses for each layer are reported in **Table S1**.

Device preparation

Commercial ITO was cleaned with oxygen plasma for 10 minutes. Afterwards, Poly(3,4-ethylenedioxythiophene):poly(styrene sulfonate) (PEDOT:PSS, PVP Al 4083) was deposited in the fume hood in ambient air by spincoating. The aqueous dispersion was first filtered using a 0.45 μm PVDF filter. 240 μL PEDOT:PSS was pipetted onto the substrate and spincoated first with 500 rpm for 10 s, then with 4000 rpm for 30 s, both steps were performed with an acceleration of 12000 rpm/s. The substrates were subsequently heated at 200 °C for 5 minutes at 200 °C in ambient conditions, after which they were taken into the glovebox to anneal for another 5 minutes at 200 °C. The substrates were then loaded into the evaporator, and 500 nm FAPb_{0.5}Sn_{0.5}I₃ perovskite films were deposited on



top as described above. After the deposition, the samples were annealed for 30 minutes at 200 °C in the glovebox. Then the samples were transferred into a different evaporation system for the deposition of a 23 nm C60 layer and a 2 nm BCP layer. Then, 100 nm silver (Ag) contacts (0.09 cm²) were deposited on top to finish the stack.

Structural characterization

X-Ray Diffraction (XRD). XRD measurements were performed on a Bruker D8 Advance-ECO diffractometer in Bragg-Brentano configuration using Cu-K α ($\lambda=1.54$ Å) radiation. The measurements were done in ambient conditions. In-situ XRD measurements were performed on a Bruker D8 Discover X-ray diffractometer in 1 bar of N₂ environment using an Anton Paar XRK900 Reactor chamber in Bragg-Brentano configuration. The measurements were performed using Cu-K α ($\lambda=1.54$ Å) and a LYNXEYE XE detector operated in 0D mode. A fixed exit slit of 0.6 mm was used, and two 0.6 mm slits were used on the secondary side.

X-Ray Photoelectron Spectroscopy (XPS). XPS measurements were done using a Thermo Scientific K-alpha system using Al-K α (1.49 keV, 8.34 Å) radiation in an ultra-high vacuum chamber (pressure < 10⁻⁸ mbar). The spot size was about 800 x 400 μm^2 , the flood gun was operated at 0.15 mA and 1 V, and the pass energy was set to 140 eV. Depth profiles were constructed by etching the layer using an Ar⁺ ion beam with an energy of 1 keV. The atomic ratios and depth profiles were obtained by fitting the XPS peaks using the ThermoAdvantage software.

Solid State Nuclear Magnetic Resonance (ssNMR). Solid-state NMR measurements were performed on a Bruker Ascend 500 magnet (B₀ = 11.7 T) with a NEO console operating at frequencies of 104.64 MHz, 125.77 MHz, and 500.16 MHz for ²⁰⁷Pb, ¹³C and ¹H respectively. Chemical shifts were referenced with respect to solid Pb(NO₃)₂ (²⁰⁷Pb -3474 ppm) and adamantane (¹H 1.81 ppm and ¹³C 38.48 ppm). The samples were packed into 3.2 mm zirconia rotors and a Bruker three channel MAS 3.2 mm DVT probe was employed. Temperatures were regulated to 25 °C for all measurements. For the ²⁰⁷Pb measurements, static spectra were recorded using the variable offset cumulative spectra (VOCS) approach. Hahn echo measurements were performed in different cumulative spectral ranges for each of the samples, varying the offset by 500 ppm each time. A 90 degree pulse length of 2.2 μs was used. An echo time of 19 μs was used for the mixed and annealed samples, while a shorter echo time of 10 μs was used for the alloy sample. Additional ²⁰⁷Pb, ¹³C and ¹H magic angle spinning NMR measurements were performed on the mixed and annealed samples. A MAS speed of 15 kHz was employed for ²⁰⁷Pb and ¹H, while 12 kHz was used for ¹³C. Here as well, ²⁰⁷Pb spectra were recorded using the Hahn-echo sequence. The ¹H spectra were recorded using the one pulse (Bloch decay) sequence, and ¹³C spectra using the hpdec sequence.

90 degree pulse lengths of 2.5 μs for ¹H and 3.5 μs for ¹³C were determined. Appropriate recycle delays were utilized based on T1, which was determined with a saturation recovery experiment.

Scanning Electron Microscopy (SEM). SEM measurements were performed on a JEOL JSM-IT700 field effect microscope with an accelerating voltage of 5 keV. Cross-sectional SEM images were obtained by attaching the samples to a stub with a 45° slope. The images were taken on a 10° angle with respect to the sample surface.

Dektak stylus profilometry. The thickness of the films was determined using stylus profilometry, performed on a Veeco Dektak 8 profilometer.

Optoelectronic characterization

Absorption measurements. Absorption spectra were collected in ambient conditions in the integrated sphere on a Lambda 1050 spectrophotometer to determine the fraction of light that was either transmitted or reflected (F_{T+R}). Subsequently, the fraction of absorbed light (F_A) was calculated by $F_A = 1 - F_{T+R}$.

Photoconductance measurements. Microwave conductivity measurements were used to study the dark conductivity, the photoconductance and the QFLS of the perovskite films. In this technique, the reduction in microwave power is directly related to a change in conductivity. Detailed information about the technique is included in the **Supporting Information**.

Cell characterization

Current density-Voltage (J-V) measurements. J-V measurements were performed by scanning between -0.1-0.9 V and measuring the current density response at a scan rate of 50 Hz using a Keithley 2604. A solar simulator (OAI TriSOLTM Large Area) was used to mimic the AM1.5 solar spectrum. The incident light intensity was 120 mW/cm².

Results

1c-sTE as a viable production method for PSC absorber layers

FAPb_{0.5}Sn_{0.5}I₃ was produced from an in-house synthesized PbSnI₃ alloy, formed by combining lead(II) iodide (PbI₂) and tin(II) iodide (SnI₂) in a 1:1 molar ratio. This alloy was sublimed first at a rate of 1.5 Å/s. In the subsequent step, a layer of formamidinium iodide (FAI) was deposited at a rate of 1.0 Å/s, following the procedure described in a previous publication.^[22] While maintaining the same deposition rates, the overall PVK film thickness was increased from 250 nm to 700 nm by proportionally scaling the individual precursor layer thicknesses without the need for additional stoichiometric optimization, as is shown in **Figure S1A**. The ability to scale up the process demonstrates the straightforward nature of the sTE process, for



which tooling factors remain constant independent of deposition time and the amount of material already deposited. After the deposition, the films were removed from the evaporator and annealed at 200 °C on a hotplate in a N₂ environment for various durations. A schematic illustration of the sTE process is included in **Figure S1B**.

It is imperative for this work to thoroughly check the interdiffusion of precursors before and after annealing, as there have been serious indications that there is a limit to the maximum film thickness that can be deposited in a single cycle (1c) using sTE with lead-based perovskites.^[30] To test the distribution of various elements across the film thickness, a compositional depth profile of a sample annealed for 10 minutes was measured using X-ray photoelectron spectroscopy (XPS) (**Figure 1A**). Most interestingly, 1c-sTE yields LBG PVK films with uniform stoichiometry throughout the entire thickness, indicating optimal interdiffusion between the PVK precursors. Even though the overall composition is constant,

the measured atomic percentages deviate somewhat from the expected values (**Table S2**), particularly an underestimation of the A- and X-site species (N and I) relative to the B-site (Sn and Pb) metals. **Table S3** presents the Pb:Sn:I ratio determined by XPS for all samples used in this study, confirming that the difference in detected halide and metal ion concentration is present throughout. These deviations are likely measurement artifacts, as nitrogen detection is known to be challenging in XPS. We also include XPS survey scans of the films' surfaces in **Figure S3** to verify that they contain no detectable impurities. Moreover, the top-view scanning electron microscopy (SEM) images in **Figure 1B** show that the films appear compact, with grains larger than 3 μm, and do not contain pinholes. The presence of continuous grains throughout the film thickness is confirmed by side-view SEM measurements (**Figure 1C**). It is noteworthy that achieving this type of film morphology via spincoating is highly challenging and typically requires extensive additive engineering.^[8,11,31,32] Collectively, the XPS and SEM

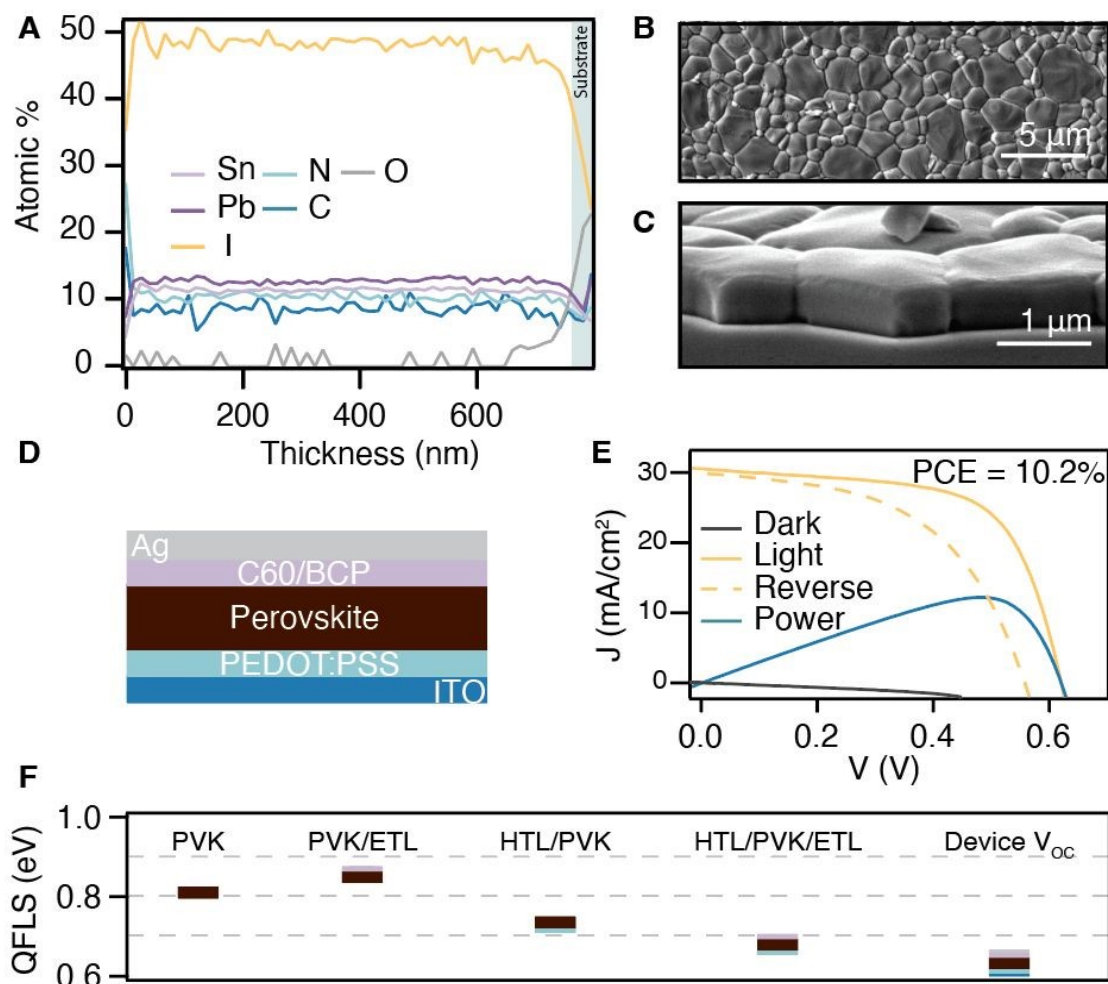


Figure 1. A. Compositional XPS depth profiles showing the atomic percentage (%) as a function of the layer thickness (nm) of FAPb_{0.5}Sn_{0.5}I₃ PVK films deposited in a single cycle of sequential thermal evaporation. B. Top-view SEM image of an annealed PVK film. The scale bar indicates 5 μm. C. Cross-sectional SEM images of an annealed PVK film. The scale bar indicates 1 μm. All samples used were annealed for 30 minutes at 200 °C. D. Schematic representation of the device architecture used in this work, consisting of ITO/PEDOT:PSS/FAPb_{0.5}Sn_{0.5}I₃/C60/BCP/Ag. E. JV and power characteristic of the champion cell employing 500 nm thick PVK films. The reverse scan is also included. F. Quasi-Fermi level splitting (QFLS) of the bare PVK film as well as the partial stacks with the HTL (PEDOT:PSS) and the ETL (C60). Plotted together with the device open-circuit voltage (V_{oc}).



results demonstrate that films fabricated using 1c-sTE are stoichiometrically homogeneous, pinhole-free, and continuous, making them ideal for PV applications.

To further demonstrate the feasibility of the 1c-sTE process, a 500 nm thick absorber layer was incorporated into a device with the architecture ITO/PEDOT:PSS/FAPb_{0.5}Sn_{0.5}I₃/C60/BCP/Ag (Figure 1D). The current-voltage characteristic of a champion cell based on this architecture, obtained using a solar simulator with an output power of 120 mW/cm², is shown in Figure 1E, yielding a power conversion efficiency (PCE) of 10.2%. This performance results from a short-circuit current density (J_{SC}) of 30.5 mA/cm², a fill factor (FF) of 65%, and an open-circuit voltage (V_{OC}) of 0.62 V. More performance parameters are included in the top row of Table S4. Although previous work from Valencia^[25] indicates that 700 nm LBG PVK layers are too thick, leading to reduced charge collection and increased parasitic absorption, we nevertheless fabricated cells with this PVK film thickness as well. A champion JV is included in Figure S4A. As expected, the increased absorption (shown for each thickness in Figure S4B) leads to a rise in current, yielding a J_{SC} of 35.2 mA/cm², while the V_{OC} and FF decrease to 0.55 eV and 61%, respectively. As is also indicated in Table S4, this results in a comparable PCE of 9.8%. While the PCE we obtain is equivalent to previously reported values for solar cells containing evaporated Pb-Sn perovskite absorbers,^[23-25] the individual performance parameters are notably different.

To identify the origin of the low device voltage and the apparent difficulties in extracting charges to the contacts, we performed QFLS measurements using light intensities comparable to 1 sun. The QFLS of bare PVK layers (0.82 eV) is compared with those of stacks incorporating an HTL, an ETL, or both. This method has been widely used in literature^[10,34-37] and is most effective for identifying voltage losses that occur at the interfaces between the PVK and the TMs. The QFLS values are also included in Table S5. Figure 1F shows that, after depositing the ETL (C60) on top, the QFLS increases slightly from 0.82 to 0.87 eV. This is an uncommon outcome, as this interface typically introduces voltage losses.^[37] In contrast, a significant voltage loss is observed when the perovskite is deposited on PEDOT:PSS (HTL), as the QFLS drops to 0.71 eV. The QFLS of the full HTL/PVK/ETL stack closely matches that of the HTL/PVK stack, reaching 0.69 eV. The remaining discrepancy between the device V_{OC} and the QFLS of the triple layer may be attributed to sheet resistance in the ITO and/or collection losses at the metal contacts. In short, the PSC produced via 1 cycle of sTE is effective, but its device architecture, particularly the selection of charge transport layers, needs improvement.

On the ease of mixing in sTE-produced FAPb_{0.5}Sn_{0.5}I₃

Having successfully integrated the 1c-produced PbSn PVKs into a PSC, we now turn to understanding the conversion, meaning the mixing of the precursors and crystallization into the PVK phase. Moreover, we investigate why these processes proceed to completion in this system,

whereas they are hampered in pure-Pb PVKs.^[30] We first compare films deposited in 1c to those prepared using a double cycle (2c) of sTE to gain insight into how the different deposition approaches influence precursor diffusion, crystallization, and the resulting film properties. In these experiments, a total thickness of 700 nm was maintained. The individual layer thicknesses are reported in Table S1. The samples were annealed at 200 °C for varying times (10 – 60 minutes).

The XRD patterns (Figure 2A and Figure 2B) show minimal differences between the two methods, with both exhibiting a preferential orientation, dominated by reflections at 14.0° and 28.2°, corresponding to the (100) and (200) crystal planes of the perovskite phase, respectively. Additionally, annealing for longer durations (> 30 mins) at 200 °C leads to the emergence of an alloy peak at 12.7°, indicating thermal degradation and reversion into the precursor. Notably, the 2c approach shows additional reflections from other crystal planes, specifically with a more pronounced (012) reflection at 31.6°. The differently oriented perovskite domains likely result from the second deposition cycle being performed on a different surface than the first. Namely, the second cycle is performed on a layer of noncrystalline FAI rather than directly on quartz. This change in substrate could influence the nucleation and growth process, thereby affecting the resulting crystal orientation.^[38,39]

Moreover, the absorbance spectra, (F_A), in Figure 2C and Figure 2D show that the bandgap of the perovskites prepared via both approaches is approximately 1.28 eV, suggesting identical compositions and phases. Interestingly, the spectra show that the 2c films require more time to convert into the same amount of absorbing material as the 1c films. In the 1c approach, the absorbance saturates after just 10 minutes of annealing, whereas full conversion in the 2c films occurs only after about 30 minutes. These findings indicate that films produced using a double cycle of sTE undergo a prolonged crystallization pathway relative to those produced via a single cycle.

The XPS depth profile of a 2c-produced sample, shown in Figure S2C, shows a similar uniformity of the elements across the film thickness, yet it differs somewhat from that of the 1c-produced film as it exhibits a higher overall formamidinium (N) content. This may be due to the second cycle being deposited on top of the first layer of FAI, which could prevent any excess material from desorbing during annealing.

The morphology of PVK layers produced via the 1c and 2c processes was further examined using top- and cross-sectional electron micrographs, provided in Figure S5 and Figure S6 for films annealed for varying durations. Similar to the 1c films, the 2c-produced layers display compact structures with no visible pinholes and feature large grains (>2 μm) across all annealing times. The 2c-produced films also exhibit columnar grains, like the 1c films, and no signs of the double cycle are visible in the film cross-section (Figure S6B). Overall, these results indicate that the film microstructure is largely comparable between the two approaches and that during annealing, the layers deposited



in separate cycles coalesce into a single grain extending throughout the entire sample thickness.

Despite the similar structural properties, bandgaps, and film morphologies, the films fabricated by these approaches display notable differences in photoconductance, which was evaluated using time-resolved microwave conductivity (TRMC) measurements. TRMC is a contactless technique that quantifies the sample conductance by measuring the decrease in

microwave power resulting from interactions with mobile carriers generated under photoexcitation, see the **Supporting Information** for a more detailed description. The photoconductance (ΔG) traces are normalized by a geometric factor (β), the elementary charge constant (e), the incident light intensity (I_0), and F_A , to express the data as a yield-mobility product. The data, presented in **Figure 2E** and **Figure 2F** for a light intensity of 10^{10} photons/cm², reveal that the 1c films

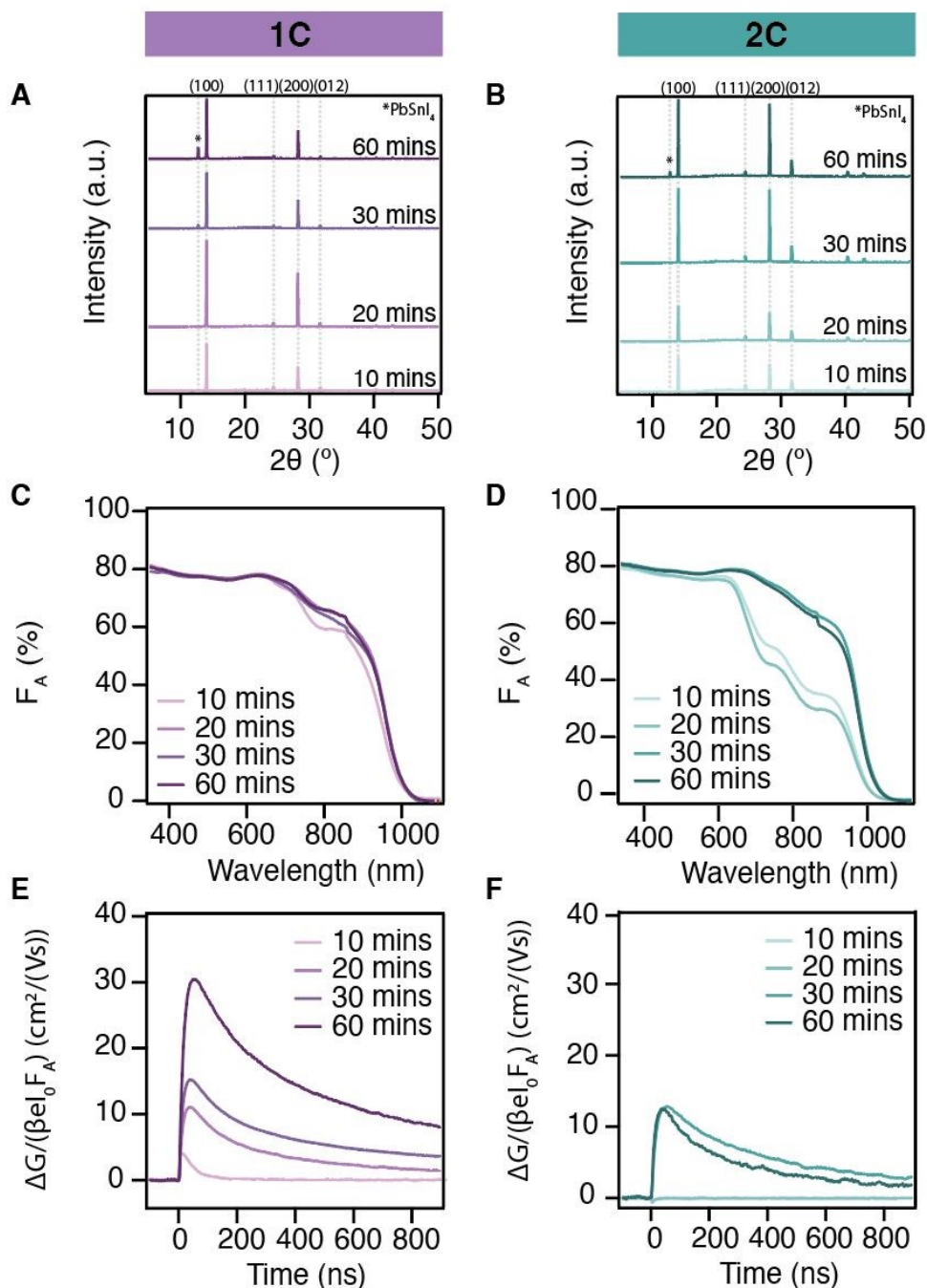


Figure 2. XRD patterns of FAPb_{0.5}Sn_{0.5}I₃ perovskite films deposited in **A.** a single cycle (1c) and **B.** a double cycle (2c) of sequential thermal evaporation. Absorption spectra, expressed as the fraction of absorbed light (F_A , %) of the **C.** 1c deposition and **D.** 2c deposition. Time-resolved photoconductance measurements of the **C.** 1c deposition and **D.** 2c deposition. The photoconductance (ΔG) is normalized by a geometric factor (β), the elementary charge constant (e), the intensity of the incoming light pulse, and F_A . All measurements were carried out on samples that were annealed for 10, 20, 30, and 60 minutes, and using light intensities of 10^{10} photons/cm².



exhibit progressively larger ΔG with annealing time, ultimately reaching maximum signals around $30 \text{ cm}^2/(\text{Vs})$. In contrast, similarly to the evolution of the absorption, the 2c films show an increase only after 20 minutes of annealing, and the maximum ΔG remains below $15 \text{ cm}^2/(\text{Vs})$.

All in all, these results demonstrate that while the 1c and 2c approaches ultimately yield structurally and morphologically comparable PVK films with similar bandgaps, their crystallization pathways differ. Counterintuitively, the 2c process exhibits slower conversion kinetics, which could be due to differences in precursor distribution during annealing. The reduced photoconductance response in the 2c films indicates that subtle differences in the films affect the electronic performance. These findings highlight that, beyond the benefits of shorter processing times and relative simplicity, the 1c-sTE films exhibit faster conversion and higher photoconductance with shorter annealing times. In this context, the homogeneous ion distribution observed in the XPS data (**Figure 1A**) raises questions regarding the diffusion and crystallization processes in these films that lead to such uniformity. To address this, we further investigate the conversion by examining the structural and optical properties at three stages of 1c production. First, we characterize a sample immediately (<15 mins) after the FAI deposition without annealing (in yellow). Another sample, denoted as mixed (in orange), was left unannealed for approximately 12 hours at room temperature in the glovebox. These layers are compared with a sample annealed for 30 minutes at 200 °C right after the FAI deposition (in burgundy). The film images included in the key (**Figure 3A**) already illustrate the extent of diffusion and crystallization at room temperature. The film's appearance changes from a bright orange hue directly after FAI deposition, characteristic of the PbSnI_4 alloy, to black by the next day. The absorption data in **Figure 3B** tell a similar story: the unannealed material initially exhibits a shallow absorption onset, which develops remarkably over the 12-hour period the film is left in the glovebox, ultimately showing a distinct onset around 1000 nm. Comparatively, the difference in absorption around the band edge between the mixed film and the annealed sample is small. The identical absorption onsets observed for PVK formed spontaneously overnight and by annealing indicate that both contain a substantial amount of $\text{FAPb}_{0.5}\text{Sn}_{0.5}\text{I}_3$. These results show that even at room temperature, diffusion and crystallization occur, yielding a PVK phase with structural and optical properties similar to the annealed films.

The conversion from precursors to the desired perovskite phase can also be followed through the structural properties using XRD. **Figure 3C** presents the diffraction patterns for the three studied samples. Directly after deposition, the film exhibits strong reflections at 12.7° , 25.5° , and 38.7° , which are characteristic of PbSnI_4 ,^[22] and only minor PVK peaks at 14.0° and 28.2° . In contrast, the mixed sample shows only the perovskite-related reflections and none of the alloy. To track the progressive diffusion and crystallization of the precursors,

the sample was monitored by XRD at 15-minute intervals (**Figure 3D**). Over a 12-hour time window, the alloy reflection at 12.7° gradually fades, while a broad (100) PVK peak at 14.0° develops. Upon annealing, the characteristic perovskite peaks remain visible in **Figure 3C**, accompanied by a small alloy peak at 12.7° , which indicates minor degradation during annealing. A magnified view of the normalized (100) reflections of the resulting PVK films is shown in **Figure 3E**. The as-deposited PVK portrays the widest peak, which narrows after mixing. Subsequent annealing for 30 minutes at 200 °C sharpens the peak, indicating an improvement in the crystallinity or increased crystallite sizes.

To study the conversion process in more detail, solid-state nuclear magnetic resonance (ssNMR) measurements were carried out to monitor the local environment of the Pb. Because mixing of the precursors occurs too rapidly, even at room temperature, in relation to the measurement time, it was not feasible to analyze an unannealed sample directly after the FAI deposition. Instead, the PbSnI_4 alloy was included. To accommodate the broad range of chemical shifts in which the NMR signal was obtained, the measurements for ^{207}Pb were performed using the variable offset cumulative spectra (VOCS) approach. The resulting static ^{207}Pb ssNMR spectra are shown in **Figure 3F-H**, plotted together with the sum of the spectra in grey. Normalized magic-angle spinning (MAS) ^1H and ^{13}C spectra are included in **Figure S7**. The PbSnI_4 ^{207}Pb spectrum exhibits a particularly broad peak spanning roughly -3000 to 4900 ppm (**Figure 3F**). After overnight mixing, the peak narrows and centers at ~ 1647 ppm. Smaller peaks appear at 0 ppm and ~ 857 ppm. Subsequent annealing results in additional narrowing, producing a sharp peak at ~ 1788 ppm.

Several factors may account for the broad chemical shift distribution observed for PbSnI_4 . For instance, variations in bond lengths or distortions of the lattice structure create asymmetric electron densities. Considering that the alloy was formed by thermally fusing PbI_2 and SnI_2 , it is expected to exhibit both compositional inhomogeneities and structural disorder. This reasoning is corroborated by the broad X-ray reflection of the alloy, spanning between 12.3° and 13.0° in **Figure 3D**, which is indicative of a distribution in lattice spacings. We attribute the main peak in **Figure 3G** to the $\text{FAPb}_{0.5}\text{Sn}_{0.5}\text{I}_3$ phase. Its higher chemical shift, which is above the ~ 1500 ppm typically reported for FAPbI_3 ,^[40,41] indicates a lower electron density surrounding the Pb nuclei. The signal around 0 ppm has previously been associated with PbI_2 ,^[41] suggesting that similar local environments may be present in our mixed material. The broad feature observed between 0 and 2000 ppm remains unidentified; it may result from sample heterogeneity, i.e., a nonuniform Pb/Sn distribution, or the possible formation of some oxide species that could have formed during transport and characterization. Regardless, annealing evidently plays a major role in enhancing the symmetry of the electron densities surrounding the Pb nuclei in the PVK, which may indicate increased symmetry in the microdistribution of Sn and Pb. This



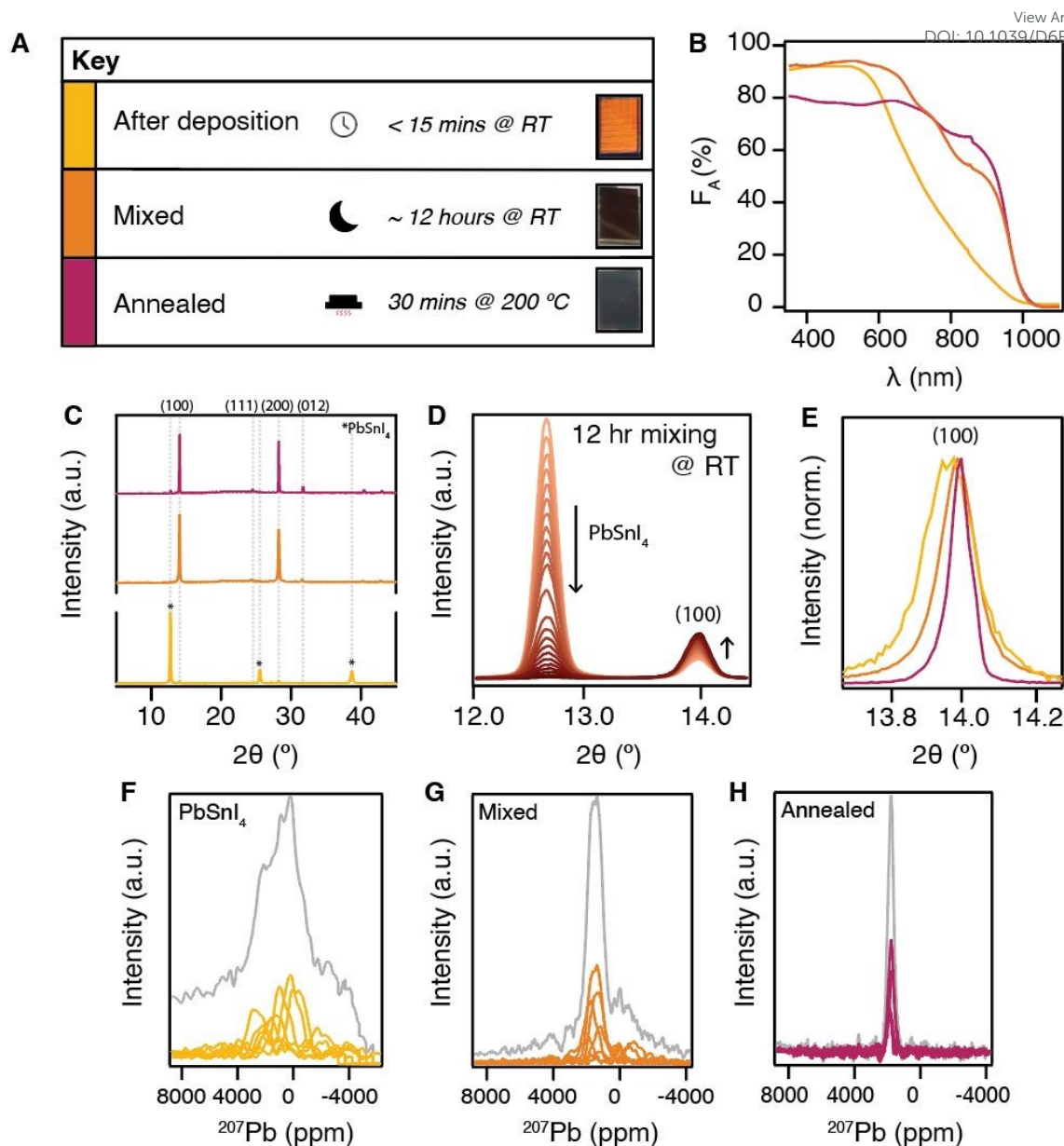


Figure 3. A. Key illustrating the different samples: a film measured within 15 minutes after the deposition (in yellow), an unannealed film left to mix overnight (in orange), and a film annealed directly after the deposition for 30 minutes at 200 °C (in burgundy). Pictures of the resulting films are also included. For all samples, the B. absorption spectra, expressed as a fraction of absorbed light (F_A) of the samples introduced in the key, and C. XRD patterns are included. D. XRD patterns, zoomed in on the alloy peak (at 12.7°) and the PVK (100) (at ~14.0°), taken every 30 minutes over the course of 12 hours while the sample was kept in a N₂ environment at room temperature (RT). E. Magnification of the (100) peak of the samples introduced in the key. Static ²⁰⁷Pb Solid-state NMR (ssNMR) spectra of F. PbSn₁₄, G. mixed, and H. annealed sample. The different spectra in each subfigure correspond to measurements with different frequency offsets to cover the wide spectral range. The sum of each of these spectra for each sample is plotted in grey.

is reflected in the substantial narrowing of the main peak in **Figure 3H** and the disappearance of the broad secondary signals.

Finally, top-view SEM images reveal pronounced changes in the films' microstructure across the different stages of the conversion. The as-deposited alloy (**Figure S8A**) exhibits a compact morphology composed of small grains (<100 nm). After overnight mixing (**Figure S8B**), the PVK film maintains the nanoscale features (<100 nm), but with visible voids distributed throughout the structure. Upon annealing, these features turn into large grains exceeding 1 μm in size (**Figure S5**).

From the combined SEM, ssNMR, XRD, and absorption results, it can be concluded that evaporated FAI can disrupt the alloy's structure sufficiently to permit complete diffusion, leaving a void-rich film with no PbSn₁₄ crystalline domains detectable by XRD. In time, a substantial amount of the desired FAPb_{0.5}Sn_{0.5}I₃ PVK phase forms even at room temperature. Nevertheless, annealing is essential to obtain PVK crystallites with a high degree of symmetry in the elemental distributions and large grains.

To further evaluate the thermodynamic stability of the PbSn₁₄ alloy and to clarify why FAI seems to diffuse so readily, detailed



DFT calculations were performed. Using the total energies from DFT, the stability of the PbSnI_4 alloy was first assessed via the synthesis reaction $\text{PbI}_2 + \text{SnI}_2 \rightarrow \text{PbSnI}_4$. This reaction has an energy change $\Delta E = -0.103$ eV, corresponding to -0.017 eV per atom, showing that the alloy is only weakly stabilized with respect to its precursors. The modest energy gain indicates that the PbSnI_4 network is thermodynamically shallow and can be readily reconfigured when additional species are introduced at the processing temperatures used here.

The perovskite $\text{FAPb}_{0.5}\text{Sn}_{0.5}\text{I}_3$ was then evaluated using the same energy reference framework. Its formation energy is $+0.0217$ eV per atom, meaning that $\text{FAPb}_{0.5}\text{Sn}_{0.5}\text{I}_3$ is only about 0.039 eV per atom less stable than the PbSnI_4 alloy. The energy difference of 0.039 eV per atom is small compared to the thermal energy available at the annealing temperature (~ 200 °C), so the alloy and perovskite have similar thermodynamic stabilities and can be interconverted under the processing conditions. Under the FAI-rich environment during deposition and annealing, entropic and interfacial effects, together with the chemical driving force for FA^+ incorporation, readily overcome this small energetic offset and enable extensive conversion of PbSnI_4 into $\text{FAPb}_{0.5}\text{Sn}_{0.5}\text{I}_3$.

This energetic picture aligns with the experimental observations that once FAI is deposited on top of the alloy, the PbSnI_4 lattice is easily disrupted. Most importantly, this allows the FAI to diffuse through the entire $500\text{--}700$ nm film, and a substantial fraction of the perovskite phase forms already during room-temperature mixing. Together, the calculations support the view that PbSnI_4 acts as a structurally soft, weakly stabilized precursor that can be converted efficiently into the mixed Pb-Sn perovskite phase during single-cycle sequential thermal evaporation.

Finally, it remains to be determined whether diffusion of FAI into PbSnI_4 is influenced by simultaneous crystallization. To address this, a sample was annealed immediately after deposition, denoted as unmixed, and compared with a sample annealed after a day of spontaneous mixing at room temperature, denoted as mixed. The different sample treatments are schematically indicated in the top panels of **Figure 4**. Given that the mixed sample already has a substantial amount of PVK and a uniform FAI distribution before annealing (see the compositional depth profiles in **Figure S2A**), no additional diffusion should be necessary for full crystallization to the PVK phase. In contrast, for the unmixed sample immediately after deposition, FAI and PbSnI_4 remain spatially separated, and mixing occurs during annealing. The difference between the samples' initial state is also evident in the two XRD patterns of the unannealed films in **Figure 4A** and **Figure 4B**, consistent with the spontaneous overnight mixing discussed in **Figure 3**. Tracking the evolution of the XRD patterns together with the photoconductance at various annealing times (0, 10, 20, 30, and 60 minutes) allows us to assess whether FAI transport during annealing influences crystallization and the resulting charge carrier dynamics.

As shown in **Figure 4A** and **Figure 4B**, the XRD patterns of the samples reveal similar diffraction peaks after annealing. In both cases, annealing for 10 minutes yields the characteristic reflections of $\text{FAPb}_{0.5}\text{Sn}_{0.5}\text{I}_3$ with no remaining alloy peaks. The alloy reflections re-emerge only after annealing for >20 minutes, indicative of thermal degradation.

From the TRMC data in **Figure 4C** and **Figure 4D**, it is evident that, for both annealing approaches, extending the annealing time to 60 minutes considerably improves the photoconductance, yielding a maximum signal around 80 $\text{cm}^2/(\text{Vs})$ at a light intensity of 9×10^{10} photons/ cm^2 . This is striking as before annealing, the films differ substantially; The unmixed sample shows basically no photoconductance immediately after deposition, while a small but persistent photoconductance signal is observed in the mixed sample, attributable to the spontaneously formed PVK (**Figure S9**). Interestingly, the evolution of the photoconductance signals with annealing time is remarkably similar for both preparation approaches. After 10 minutes of annealing, the signal peaks at $2\text{--}3$ $\text{cm}^2/(\text{Vs})$ and increases to $15\text{--}25$ $\text{cm}^2/(\text{Vs})$ after 20 minutes. Here, lifetimes of around $150\text{--}250$ ns are observed. At 30 minutes of annealing, the photoconductance decreases slightly, yet the carrier lifetimes extend to 700 ns. Further annealing to a total of 60 minutes increases the signal height and prolongs the lifetimes to beyond 4 μs , as shown more clearly in **Figure S9**. This enhancement correlates with the reappearance of the PbSnI_4 alloy peak at 12.7° in the XRD pattern in **Figure 4A** and **Figure 4B**. An excess of inorganic precursor has been associated with effective grain boundary passivation, resulting in longer-living photoconductance signals, albeit typically accompanied by lower device performances.^[42-44]

The TRMC data also contains information regarding the defect density in the material. **Figure S10** presents TRMC signals for both samples, recorded at different light intensities. After 10 minutes of annealing, the rapidly decaying traces overlap across all excitation intensities. This behavior indicates that the charge carrier generation density remains below the trap density of the film, resulting in the same transient photoconductance signals regardless of the applied laser intensity.^[45] Accordingly, the trap density can be estimated from the laser pulse intensity at which the traces stop to overlap. In this case, after correcting for the sample thickness, we find this to be greater than 10^{15} cm^{-3} . With annealing times beyond 10 minutes, the traces no longer overlap. Instead, the signals lower altogether with increasing laser pulse intensity. This suggests the emergence of a dominant second-order band-to-band recombination, which occurs once the trap density has been exceeded. Hence, it can be concluded that the trap density lowers significantly from $>10^{15}$ cm^{-3} to around 10^{13} cm^{-3} upon annealing. This trend is observed for films produced via both approaches presented in **Figure 4**.



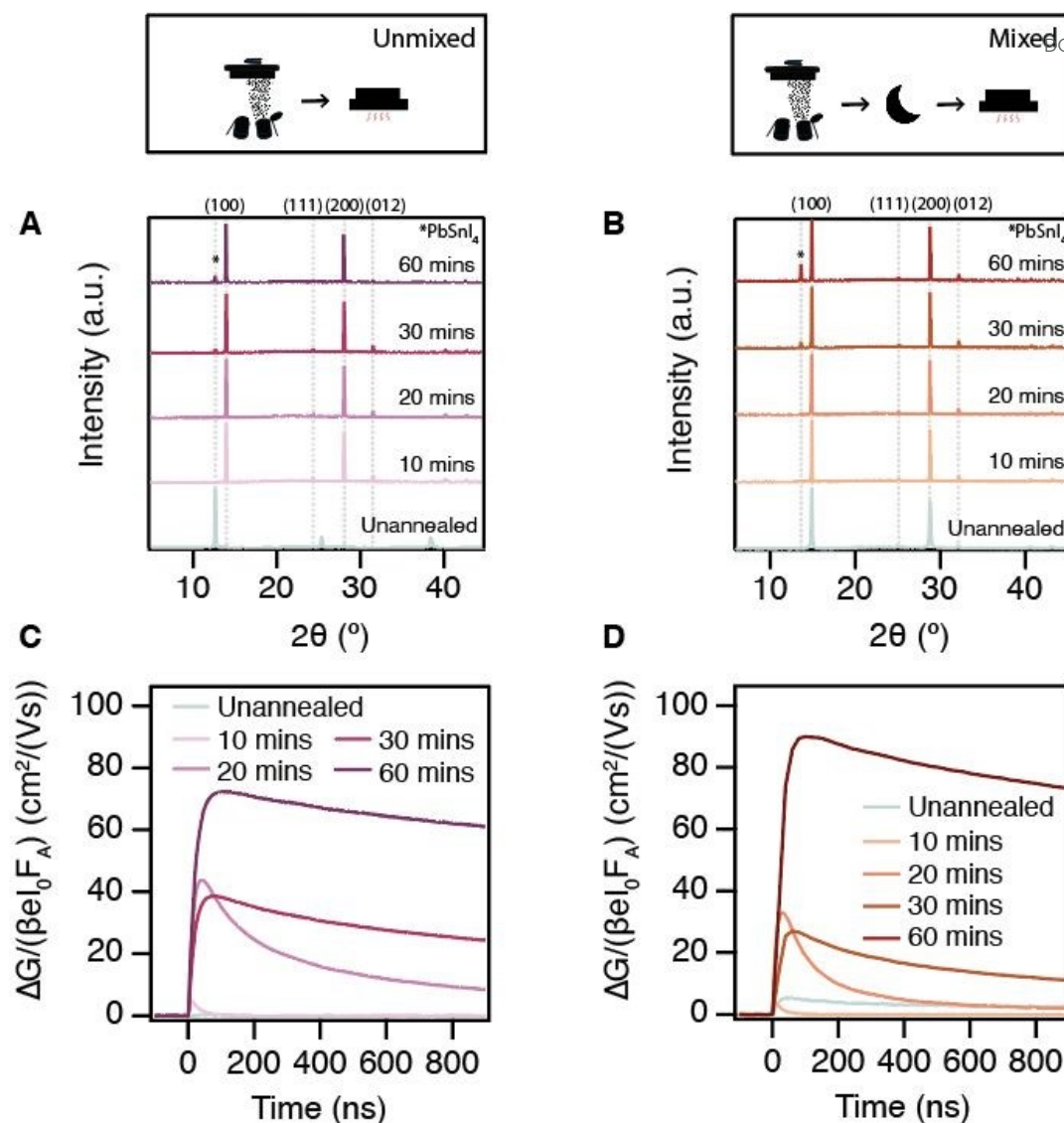


Figure 4. XRD patterns of perovskite films left unannealed and annealed at 200 °C for varying times **A.** immediately after the deposition, and **B.** after overnight mixing. Photoconductance traces as a function of time for perovskite films annealed at 200 °C, **C.** immediately after the deposition, and **D.** after overnight mixing. The annealing timing is also schematically indicated in the panels above the TRMC traces. The ΔG signals are reported for different annealing times (10, 20, 30 and 60 minutes) and using a light intensity of 9×10^{10} photons/cm².

Additional information about the annealing process in the films is provided by dark microwave conductivity (DMC) measurements, in which the GHz response is recorded as a function of resonance frequency. As shown in **Figure S11**, a clear difference in microwave interactions is observed between the unannealed samples. For the unmixed sample, the normalized resonance dip reaches a minimum of approximately 0.63, whereas for the mixed sample, the dip deepens to 0.39. Dip deepening in DMC is associated with increased background conductivity. Upon annealing, the resonance dips in both cases shift to approximately 0.51 after 10 minutes and subsequently become shallower, reaching around 0.6 after 60 minutes. This is comparable to the substrate, implying that annealing reduces the background conductivities to < 1 S/m. From this and the fact that the charge carrier mobility only increases, we can conclude

that the initially present doping concentrations, in particular for the mixed sample, are neutralized by the annealing process.

Based on the similarities in the evolution of the TRMC signals and structural properties during annealing, we can infer that the PVK films are in equivalent stages of conversion at each time step. Hence, the diffusion is not significantly hampered by simultaneous crystallization and is either very rapid or proceeds independently of the crystallization process at these high temperatures.

Despite the close agreement in diffraction patterns and transient photoconductance, we decided to fabricate PSCs using the mixed PVK films. The JV characteristic of a champion device is included in **Figure S12A**. In line with the TRMC findings, the two fabrication approaches yield nearly indistinguishable performance. The devices based on mixed PVK layers achieve a champion PCE of 10.3%, composed of a J_{SC} of 30.9 mA/cm², a



V_{OC} of 0.61 V, and a FF of 66%. The device parameters are also included in **Table S4**. Likewise, we find almost identical QFLS values for both deposition approaches for the bare PVK film as well as the PVK/ETL, HTL/PVK, and HTL/PVK/ETL stacks, which are also included in **Figure S12B** and listed in **Table S5**. As noted above, the major voltage losses appear at the HTL/PVK interface. In the future, approaches incorporating carbazole-based materials like ((2-(9H-carbazol-9-yl)ethyl)phosphonic acid (2PACz), which have recently shown significant success,^[46,47] represent a more promising approach.

Taken together, the findings on the diffusion and crystallization presented in **Figure 3** and **Figure 4** indicate that FAI and $PbSn_4$ readily mix and convert into the PVK phase at room temperature, consistent with the thermodynamically shallow stability of this system. Although the mixed PVK is macroscopically homogeneous, as evidenced by X-ray reflections and a uniform elemental distribution throughout the film's thickness, it is modestly doped. For both samples, annealing is required to achieve films with increased local homogeneity, large grains, and high crystallinity. These structural changes lead to a reduction in defect density and increased carrier mobility, along with longer lifetimes. For mixed samples, annealing substantially reduces the background conductivity. Hence, for electronic activation, high temperatures are essential. We speculate that this is related to the repositioning of the larger, less mobile ions, such as Sn^{2+} and Pb^{2+} , to improve the elemental distribution at the microscale.

Conclusion

All in all, we demonstrate the scalable fabrication of low bandgap Pb-Sn perovskite films up to 700 nm thick using a single cycle of sequential thermal evaporation. The resulting films are stoichiometrically uniform throughout their thickness and exhibit large, columnar grains with a compact morphology. A detailed investigation of the crystallization and diffusion processes during the production of these perovskites revealed that, after the vacuum deposition, the precursors readily mix when the samples are left in the glovebox overnight. Additionally, the desired $FAPb_{0.5}Sn_{0.5}I_3$ phase gradually forms over time. We attribute this behavior to the relatively weak thermodynamic stabilization of the PVK phase compared to the precursors. Moreover, we conclude that annealing is essential to achieve films with improved elemental homogeneity on basis of the ssNMR, large grains, and high crystallinity. These improvements lead to reduced defect density, increased carrier mobilities up to $80 \text{ cm}^2/(\text{Vs})$, and longer lifetimes as determined by dark and time-resolved microwave techniques. When integrated into solar cells with the architecture ITO/PEDOT:PSS/ $FAPb_{0.5}Sn_{0.5}I_3$ /C60/BCP/Ag, they achieved champion efficiencies of 10.3%, with observed voltage losses predominantly originating from the interface with the PEDOT:PSS HTL. In conclusion, this work contributes to the development of large-scale fabrication methods for low

bandgap perovskite films using thermal evaporation, highlighting their potential for commercialization as high-performance absorber layers.

Author contributions

L.P., A.S., and T.S. designed and supervised the project. M.D. and L.P. prepared the samples, with the assistance of R.B and N.S., and measured XRD, UVVIS, SEM, XPS, IV, and microwave conductivity measurements. L.B. and L.P. measured in-situ XRD. P.V and D.G. performed and analyzed the DFT calculations. S.G and L.B. performed and analyzed the ssNMR measurements. L.P and T.S. wrote the manuscript, with the input of the remaining authors.

Conflicts of interest

There are no conflicts to declare.

Data availability

The data supporting this article have been included as part of the Supplementary Information. Supplementary information: Tables S1-S5, Figures S1-S12, and further experimental details regarding the TRMC measurements. See DOI: [URL – format <https://doi.org/DOI>]

Acknowledgements

The acknowledgements come at the end of an article after the conclusions and before the notes and references.

Notes and references

- 1 National Renewable Energy Laboratory. *Best Research-Cell Efficiencies*, <<https://www.nrel.gov/pv/cell-efficiency.html>> (2023).
- 2 Lin, R. *et al.* All-perovskite tandem solar cells with 3D/3D bilayer perovskite heterojunction. *Nature* **620**, 994-1000 (2023). <https://doi.org/10.1038/s41586-023-06278-z>
- 3 Liu, J. *et al.* Perovskite/silicon tandem solar cells with bilayer interface passivation *Nature* **635**, 596-603 (2024). <https://doi.org/10.1038/s41586-024-07997-7>
- 4 Liu, X. *et al.* Charge carrier management for highly efficient perovskite/Si tandem solar cells with poly-Si based passivating contacts. *Energy & Environmental Science* **18**, 5599-5609 (2025). <https://doi.org/10.1039/d5ee01486g>
- 5 Liu, Z. *et al.* All-perovskite tandem solar cells achieving >29% efficiency with improved (100) orientation in wide-bandgap perovskites. *Nature Materials* **24**, 252-259 (2025). <https://doi.org/10.1038/s41563-024-02073-x>
- 6 Huang, F., Li, M., Siffalovic, P., Cao, G. & Tian, J. From scalable solution fabrication of perovskite films towards commercialization of solar cells. *Energy & Environmental Science* **12**, 518-549 (2019). <https://doi.org/10.1039/c8ee03025a>



- 7 Zhao, Y. *et al.* Research progress in large-area perovskite solar cells. *Photonics Research* **8**, 1848-1865 (2020). <https://doi.org/10.1364/prj.392996>
- 8 Saki, Z., Byranvand, M. M., Taghavinia, N., Kedia, M. & Saliba, M. Solution-processed perovskite thin-films: the journey from lab- to large-scale solar cells. *Energy & Environmental Science* **14**, 5690-5722 (2021). <https://doi.org/10.1039/d1ee02018h>
- 9 Yang, F. *et al.* Upscaling Solution-Processed Perovskite Photovoltaics. *Advanced Energy Materials* **11**, 2101973 (2021). <https://doi.org/10.1002/aenm.202101973>
- 10 Zhang, K. *et al.* Suppressing Nonradiative Recombination in Lead-Tin Perovskite Solar Cells through Bulk and Surface Passivation to Reduce Open Circuit Voltage Losses. *ACS Energy Letters* **7**, 3235-3243 (2022). <https://doi.org/10.1021/acseenergylett.2c01605>
- 11 Lee, H., Kang, S. B., Lee, S., Zhu, K. & Kim, D. H. Progress and outlook of Sn-Pb mixed perovskite solar cells. *Nano Convergence* **10**, 21 (2023). <https://doi.org/10.1186/s40580-023-00371-9>
- 12 Wang, H. *et al.* Additive Engineering for Mixed Lead-Tin Narrow-Band-Gap Perovskite Solar Cells: Recent Advances and Perspectives. *Energy & Fuels* **37**, 6401-6423 (2023). <https://doi.org/10.1021/acs.energyfuels.3c00462>
- 13 Yan, J., Savenije, T. J., Mazzarella, L. & Isabella, O. Progress and challenges on scaling up of perovskite solar cell technology. *Sustainable Energy & Fuels* **6**, 243-266 (2022). <https://doi.org/10.1039/d1se01045j>
- 14 Vaynzof, Y. The Future of Perovskite Photovoltaics—Thermal Evaporation or Solution Processing? *Advanced Energy Materials* **10**, 2003073 (2020). <https://doi.org/10.1002/aenm.202003073>
- 15 Wang, Z. *et al.* Thermally Evaporated Metal Halide Perovskites and Their Analogues: Film Fabrication, Applications and Beyond. *Small Methods* **9**, 24001633 (2024). <https://doi.org/10.1002/smtd.202301633>
- 16 Feeny, T. *et al.* High-Rate FA-Based Co-Evaporated Perovskites: Understanding Rate Limitations and Practical Considerations to Overcome Their Impact. *Advanced Functional Materials* **35**, 2517873 (2025). <https://doi.org/10.1002/adfm.202517873>
- 17 Boekhoff, R. K. *et al.* Interplay of cross-reading, pressure and co-evaporation speed on triple-source FA-based perovskite films and devices. *Chemical Engineering Journal* **530**, 173755 (2026). <https://doi.org/10.1016/j.cej.2026.173755>
- 18 Momblona, C. *et al.* Efficient vacuum deposited p-i-n and n-i-p perovskite solar cells employing doped charge transport layers. *Energy Environ. Sci.* **9**, 3456-3463 (2016). <https://doi.org/10.1039/c6ee02100j>
- 19 Li, J. *et al.* Highly Efficient Thermally Co-evaporated Perovskite Solar Cells and Mini-modules. *Joule* **4**, 1035-1053 (2020). <https://doi.org/10.1016/j.joule.2020.03.005>
- 20 Ross, M. *et al.* Co-Evaporated p-i-n Perovskite Solar Cells beyond 20% Efficiency: Impact of Substrate Temperature and Hole-Transport Layer. *ACS Appl Mater Interfaces* **12**, 39261-39272 (2020). <https://doi.org/10.1021/acsami.0c10898>
- 21 Li, H. *et al.* Sequential vacuum-evaporated perovskite solar cells with more than 24% efficiency. *Science Advances* **8**, eabn8917 (2022). <https://doi.org/DOI:10.1126/sciadv.abo7422>
- 22 van der Poll, L. M. *et al.* Additive-Free Sequential Thermal Evaporation of Near-Intrinsic Pb-Sn Perovskites. *Small Methods* **9**, 2401246 (2024). <https://doi.org/10.1002/smtd.202401246>
- 23 Ball, J. M. *et al.* Dual-Source Coevaporation of Low-Bandgap FA_{1-x}Cs_xSn_{1-y}Pb_yI₃ Perovskites for Photovoltaics. *ACS Energy Letters* **4**, 2748-2756 (2019). <https://doi.org/10.1021/acseenergylett.9b01855>
- 24 Igual-Muñoz, A. M., Ávila, J., Boix, P. P. & Bolink, H. J. FAPb_{0.5}Sn_{0.5}I₃: A Narrow Bandgap Perovskite Synthesized through Evaporation Methods for Solar Cell Applications. *Solar RRL* **4**, 1900283 (2020). <https://doi.org/10.1002/solr.201900283>
- 25 Igual-Muñoz, A. M., Castillo, A., Dreesen, C., Boix, P. P. & Bolink, H. J. Vacuum-Deposited Multication Tin-Lead Perovskite Solar Cells. *ACS Applied Energy Materials* **3**, 2755-2761 (2020). <https://doi.org/10.1021/acsaem.9b02413>
- 26 Savill, K. J. *et al.* Impact of Tin Fluoride Additive on the Properties of Mixed Tin-Lead Iodide Perovskite Semiconductors. *Advanced Functional Materials* **30**, 2005594 (2020). <https://doi.org/10.1002/adfm.202005594>
- 27 Chen, Q. *et al.* Unveiling Roles of Tin Fluoride Additives in High-Efficiency Low-Bandgap Mixed Tin-Lead Perovskite Solar Cells. *Advanced Energy Materials* **11**, 2101045 (2021). <https://doi.org/10.1002/aenm.202101045>
- 28 Nespola, J. *et al.* Quantitative Analysis of the Doping and Defect Density in Mixed Sn-Pb Perovskites Mediated by SnF₂. *Chemistry of Materials* **37**, 7611-7621 (2025). <https://doi.org/10.1021/acs.chemmater.5c00816>
- 29 Yuan, H. *et al.* A tin fluoride-free, efficient and durable tin-lead perovskite solar cell. *Nature Communications* **17** (2026). <https://doi.org/10.1038/s41467-025-65445-0>
- 30 Yan, J. *et al.* Crystallization Process for High-Quality Cs_{0.15}FA_{0.85}PbI_{2.85}Br_{0.15} Film Deposited via Simplified Sequential Vacuum Evaporation. *ACS Applied Energy Materials* **6**, 10265-10273 (2023). <https://doi.org/10.1021/acsaem.3c00203>
- 31 Dong, Y. *et al.* Crystal Growth Modulation of Tin-Lead Halide Perovskites via Chaotropic Agent. *Journal of the American Chemical Society* **147**, 31578-31590 (2025). <https://doi.org/10.1021/jacs.5c05772>
- 32 Poli, I. *et al.* DMSO-Free Processing of Tin-Lead Perovskite Thin Films for Solar Cells with Enhanced Stability. *ACS Energy Letters* **11**, 3416 (2026). <https://doi.org/10.1021/acseenergylett.5c03416>
- 33 Li, C. *et al.* Diamine chelates for increased stability in mixed Sn-Pb and all-perovskite tandem solar cells. *Nature Energy* **9**, 1388-1396 (2024). <https://doi.org/10.1038/s41560-024-01613-8>
- 34 Caprioglio, P. *et al.* On the Relation between the Open-Circuit Voltage and Quasi-Fermi Level Splitting in Efficient Perovskite Solar Cells. *Advanced Energy Materials* **9**, 1901631 (2019). <https://doi.org/10.1002/aenm.201901631>
- 35 Caprioglio, P. *et al.* On the Origin of the Ideality Factor in Perovskite Solar Cells. *Advanced Energy Materials* **10**, 2000502 (2020). <https://doi.org/10.1002/aenm.202000502>
- 36 Caprioglio, P. *et al.* Open-circuit and short-circuit loss management in wide-gap perovskite p-i-n solar cells. *Nat*



Commun **14**, 932 (2023). <https://doi.org/10.1038/s41467-023-36141-8>

37 Warby, J. *et al.* Understanding Performance Limiting Interfacial Recombination in pin Perovskite Solar Cells. *Advanced Energy Materials* **12**, 21103567 (2022). <https://doi.org/10.1002/aenm.202103567>

38 Yan, J. *et al.* Vacuum Deposited Perovskites with a Controllable Crystal Orientation. *J Phys Chem Lett* **14**, 8787-8795 (2023). <https://doi.org/10.1021/acs.jpcllett.3c01920>

39 Wang, Z. *et al.* Frank-van der Merwe-Mediated Sequential Thermal Evaporation for Stable FASnI₃ Perovskite Solar Cells. *ACS Nano* **20**, 1159-1169 (2025). <https://doi.org/10.1021/acsnano.5c16992>

40 Ha, M. *et al.* Phase Evolution in Methylammonium Tin Halide Perovskites with Variable Temperature Solid-State ¹¹⁹Sr NMR Spectroscopy. *The Journal of Physical Chemistry C* **124**, 15015-15027 (2020). <https://doi.org/10.1021/acs.jpcc.0c03589>

41 Piveteau, L., Morad, V. & Kovalenko, M. V. Solid-State NMR and NQR Spectroscopy of Lead-Halide Perovskite Materials. *Journal of the American Chemical Society* **142**, 19413-19437 (2020). <https://doi.org/10.1021/jacs.0c07338>

42 Jacobsson, T. J. *et al.* Unreacted PbI₂ as a Double-Edged Sword for Enhancing the Performance of Perovskite Solar Cells. *Journal of the American Chemical Society* **138**, 10331-10343 (2016). <https://doi.org/10.1021/jacs.6b06320>

43 Liu, F. *et al.* Is Excess PbI₂ Beneficial for Perovskite Solar Cell Performance? *Advanced Energy Materials* **6**, 1502206 (2016). <https://doi.org/10.1002/aenm.201502206>

44 Gao, Y., Raza, H., Zhang, Z., Chen, W. & Liu, Z. Rethinking the Role of Excess/Residual Lead Iodide in Perovskite Solar Cells. *Advanced Functional Materials* **33**, 2215171 (2023). <https://doi.org/10.1002/adfm.202215171>

45 Savenije, T. J., Guo, D., Caselli, V. M. & Hutter, E. M. Quantifying Charge Carrier Mobilities and Recombination Rates in Metal Halide Perovskites from Time-Resolved Microwave Photo-conductivity Measurements. *Advanced Energy Materials* **10**, 2000448 (2020).

46 Sun, Y., Lai, Y. & Yang, Y. Progress of Hole-Transport Layers in Mixed Sn-Pb Perovskite Solar Cells. *Small* **20**, 2406991 (2024). <https://doi.org/10.1002/sml.202406991>

47 Zhumagali, S. *et al.* Efficient Narrow Bandgap Pb-Sn Perovskite Solar Cells Through Self-Assembled Hole Transport Layer with Ionic Head. *Advanced Energy Materials* **15**, 2404617 (2025). <https://doi.org/10.1002/aenm.202404617>

View Article Online
DOI: 10.1039/D6EL00044D



Data availability statement (also included in manuscript)

The data supporting this article have been included as part of the Supplementary Information. Supplementary information: Tables S1-S4, Figures S1-S12, and further experimental details regarding the TRMC measurements. See DOI: [URL – format <https://doi.org/DOI>]

